

Sketched Equivariant Imaging Regularization and Deep Internal Learning for Inverse Problems

Guixian Xu

*School of Mathematics,
University of Birmingham*

GXX422@STUDENT.BHAM.AC.UK

Jinglai Li

*School of Mathematics,
University of Birmingham*

J.LI.10@BHAM.AC.UK

Junqi Tang

*School of Mathematics,
University of Birmingham*

J.TANG.2@BHAM.AC.UK

Abstract

Equivariant Imaging (EI) regularization has become the de-facto technique for unsupervised training of deep imaging networks, without any need of ground-truth data. Observing that the EI-based unsupervised training paradigm currently has significant computational redundancy leading to inefficiency in high-dimensional applications, we propose a sketched EI regularization which leverages the randomized sketching techniques for acceleration. We apply our sketched EI regularization to develop an accelerated deep internal learning framework, which can be efficiently applied for test-time network adaptation. Additionally, for network adaptation tasks, we propose a parameter-efficient approach to accelerate both EI and Sketched-EI via optimizing only the normalization layers. Our numerical study on X-ray CT and multicoil magnetic resonance image reconstruction tasks demonstrate that our approach can achieve significant computational acceleration over standard EI counterpart in single-input setting and network adaptation at test time.

1. Introduction

Unsupervised training has become a vital research direction for imaging inverse problems (Carioni et al., 2024; Tirer et al., 2024). For the most popular and widely applied medical imaging applications such as CT/MRI/PET, such strategies seek to train deep reconstruction network from only the noisy and incomplete measurement data:

$$y = Ax^\dagger + \varepsilon, \quad (1)$$

where we denote here $x^\dagger \in \mathbb{R}^d$ as the ground-truth image (to be estimated), $A \in \mathbb{R}^{n \times d}$ as the measurement operator, $\varepsilon \in \mathbb{R}^n$ as the measurement noise, while $y \in \mathbb{R}^n$ as the measurement data. To be more precise, such unsupervised training schemes typically seek to learn a reconstruction network (set of network parameters denoted as θ here)

$$\mathcal{F}_\theta(A^\dagger y) \rightarrow x \quad (2)$$

with only the knowledge of the measurement data y and the measurement operator A . Here we denote A^\dagger as the pseudo-inverse of A , or a stable approximation of it (such as the FBP for X-ray CT). This line of research initialized on the Deep Internal Learning schemes (see recent review paper by [Tirer et al. \(2024\)](#)) such as the Deep Image Prior (DIP) approach ([Ulyanov et al., 2018](#); [Tachella et al., 2021](#); [Mataev et al., 2019](#); [Liu et al., 2019](#)) for learning image reconstruction from single input, and more recently the Noise2X-type approaches ([Lehtinen et al., 2018](#); [Batson and Royer, 2019](#)), and its extension Artifact2Artifact ([Liu et al., 2020](#)). The most successful unsupervised training paradigm is currently the Equivariant Imaging (EI) regularization proposed by ([Chen et al., 2021, 2022](#); [Tachella et al., 2023](#)), which is able to enforce the network to learn beyond the range space of the measurement operator A and fully achieving ground-truth-free training under incomplete and noisy measurements. Compared to standard supervised training which requires ground-truth and measurement pairs, unsupervised training, in general, is computationally much more costly. This is due to the fact that the forward/adjoint/pseudoinverse operators are computed in each iteration of the training optimizer, leading to significant computational overhead. In this work, we take an initial yet crucial step for mitigating the computational limitation of unsupervised training schemes for deep imaging networks, by accelerating EI regularization via dimensionality reduction (sketching) techniques rooted in stochastic optimization.

1.1 Background

Deep Internal Learning. The most typical and fundamental deep internal learning scheme is the deep imaging prior (DIP) approach proposed by ([Ulyanov et al., 2018](#)). The DIP can be described as approximately minimizing the following loss by first-order optimizers such as SGD or Adam:

$$\begin{aligned}\theta^* &\approx \arg \min_{\theta} \|y - A\mathcal{F}_{\theta}(z)\|_2^2, \\ x^* &= \mathcal{F}_{\theta^*}(z),\end{aligned}\tag{3}$$

where the input z can be chosen as random vector or $z = A^\dagger y$ for warm-starting ([Tachella et al., 2021](#)). In its vanilla form, it takes a randomly initialized deep convolutional network and trains it directly on the given single measurement data. Perhaps surprisingly, the vanilla version of DIP can already provide excellent reconstruction performance on many inverse problems such as image denoising/superresolution/deblurring and tomographic image reconstruction tasks such as CT/MRI/PET ([Singh et al., 2023](#); [Mayo et al., 2024](#)).

In addition to learning reconstruction from a single input, DIP can also be effectively applied for network adaptation at the test time against distribution shifts ([Barbano et al., 2022](#)). Suppose given a pre-trained reconstruction network on a certain set of measurements y and operator A , if we apply directly the network to a different inverse problem with a new A' which has fewer measurements and noisier y' , the pre-trained network can perform badly. However, one can mitigate this distribution shift by adapting the network via the DIP framework above or regularized versions of DIP such as the DIP-GSURE approach by [Abu-Hussein et al. \(2022\)](#).

Equivariant Imaging Regularization. Among all the unsupervised approaches for training deep imaging networks, the EI framework proposed by [Chen et al. \(2021, 2022\)](#) was the first to explicitly address the issue of learning beyond the range space of the forward operator A using the inherent symmetric structures of the imaging systems. Given a collection of measurements Y , and group transformation T_g tailored for the imaging systems (for example, rotation for CT), the vanilla EI framework can be written as:

$$\theta^* \approx \arg \min_{\theta} f_{\text{EI}}(\theta) := \underbrace{\mathbb{E}_{g \sim G, y \sim Y} \{\|y - A(\mathcal{F}_{\theta}(A^\dagger y))\|_2^2\}}_{\text{MC loss}} + \lambda \underbrace{\|T_g \mathcal{F}_{\theta}(A^\dagger y) - \mathcal{F}_{\theta}(A^\dagger A T_g \mathcal{F}_{\theta}(A^\dagger y))\|_2^2}_{\text{EI regularization}},\tag{4}$$

where the first term is the measurement-consistency loss, while the second term is the EI regularizer which enable the training program to learn in the null-space of A . After this first pivoting work, variants of EI have been developed to enhance the robustness to measurement noise, using an additional G-SURE (Chen et al., 2022) or UNSURE (Tachella et al., 2024) regularizer alongside with EI. Meanwhile, extensions of EI on new group actions tailored for different inverse problems have been proposed (Wang and Davies, 2024b,a; Scanvic et al., 2023). In our work, we focus on sketching the vanilla form of the EI regularizer, but the same principle can be easily extended for all these enhanced versions of EI.

Randomized Sketching and Stochastic Optimization. Operator sketching and stochastic gradient-based optimization techniques have been widely applied for machine learning (Kingma and Ba, 2015; Johnson and Zhang, 2013; Pilanci and Wainwright, 2015, 2017; Tang et al., 2017) and more recently in imaging inverse problems (Sun et al., 2019; Ehrhardt et al., 2024). In the context of imaging inverse problems, given a measurement consistency loss $\arg \min_x \|Ax - y\|_2^2$, one can split the objective function in to N partition of minibatches:

$$\|Ax - y\|_2^2 = \sum_{i=1}^N \|S_i Ax - S_i y\|_2^2$$

where S_i are the set of sketching operators (typically sub-sampling for imaging applications). After splitting the objective function into minibatches, one can use stochastic gradient methods as the optimizer for efficiency. In a pioneering work of Tang et al. (2020), they demonstrate that the success of stochastic optimization and operator sketching techniques depends on the spectral structure of the forward operator A . If A has a fast decay in the singular value spectrum, then we can expect an order-of-magnitude acceleration in terms of computational complexity over deterministic methods such as proximal gradient descent or FISTA (Beck and Teboulle, 2009). Most of the computationally intensive imaging inverse problems fall into this category, for example, X-ray CT, multi-coil MRI and Positron Emission Tomography all admit efficient applications of operator sketching and stochastic optimization. In our work here, we leverage operator sketching for the acceleration of EI-regularization and jointly with the DIP measurement consistency.

1.2 Contributions

The contribution of our work is four-fold:

- **Sketched EI regularization** – We propose an efficient variant of the EI regularizer, mitigating the computational inefficiency of the original approach by (Chen et al., 2021). We provide a motivational theoretical analysis on the approximation bound of our sketched EI regularizer, demonstrating that our approach admits a nice mathematical interpretation.
- **Sketched EI-based test-time network adaptation with application in X-ray CT** – Based on our sketched EI regularizer, jointly with sketching on measurement consistency term, we propose an efficient deep internal learning framework, for single-input / task-adapted image reconstruction, and test-time network-adaptation. We apply our Sketched-EI approach in sparse-view X-ray CT imaging tasks and demonstrate significant computational acceleration over standard EI.
- **Coil-sketched EI for multi-coil MRI** – For a special but important medical imaging application, multicoil MRI, we design a special variant of sketched EI that utilizes the coil-sketching technique (Oscanoa et al., 2024). We numerically observe a striking “less is more” effect (Rudi et al., 2015), that is, our coil-sketched EI can significantly improve both the reconstruction accuracy and computational

complexity at the same time over standard EI due to an implicit regularization effect of this tailored dimensionality reduction.

- **Parameter-efficient network adaptation** – Building on the EI and Sketched EI framework, we propose an even more computationally efficient approach for network adaptation, which takes a pre-trained network and fine-tunes on the given inverse problem at hand. Our new approaches (BN-EI and BN-Sk-EI) select only a fraction of the network parameters (which typically are the Batch-Norm layers) on the EI and Sketched EI. Our numerical results demonstrate the remarkable computational efficiency of this strategy in accelerating both the original EI and the sketched EI.

2. Sketched Equivariant Imaging Regularization and Deep Internal Learning

In this section, we present our sketching scheme for the EI regularizer and the resulting Sketched EI regularization approach for single-input deep internal learning, and test-time network adaptation. We also propose a very efficient approach for accelerating both EI and Sketched EI for network adaptation at test time, via optimizing only the parameters of normalization layers. Meanwhile, we provide a theoretical analysis that reveals the motivation of this scheme for further insights.

2.1 Algorithmic Framework of Sketched EI Regularization

The EI-regularized unsupervised learning is much more computationally inefficient compared to supervised training, due to the need of computing the measurement operator multiple times in every training iterations. Observing that there is significant computational redundancy in the EI-regularizer, we propose a sketched EI regularizer, which replaces A and A^\dagger with sketched minibatches $A_S := SA$ and $A_S^\dagger := (SA)^\dagger$, where $S \in \mathbb{R}^{m \times d}$ is a random sketching operator satisfying $\mathbb{E}(S^T S) = I$. In imaging inverse problems, we can simply choose M to be a sub-sampling operator:

$$\mathbb{E}_{g \sim G, M} \|T_g \mathcal{F}_\theta(A^\dagger y) - \mathcal{F}_\theta(A_S^\dagger A_S T_g \mathcal{F}_\theta(A^\dagger y))\|_2^2 \approx \mathbb{E}_{g \sim G} \|T_g \mathcal{F}_\theta(A^\dagger y) - \mathcal{F}_\theta(A^\dagger A T_g \mathcal{F}_\theta(A^\dagger y))\|_2^2. \quad (5)$$

Jointly performing the sketch in the measurement consistency term with $y_S := S y$, we can derive our Sketched EI framework as follows:

$$\theta^* \approx \arg \min_{\theta} f_{\text{Sk.EI}}(\theta) := \mathbb{E}_{y \sim Y, g \sim G, S} \left\{ \underbrace{\|y_S - A_S(\mathcal{F}_\theta(A^\dagger y))\|_2^2}_{\text{Sketched MC loss}} + \lambda \underbrace{\|T_g \mathcal{F}_\theta(A^\dagger y) - \mathcal{F}_\theta(A_S^\dagger A_S T_g \mathcal{F}_\theta(A^\dagger y))\|_2^2}_{\text{Sketched EI regularization}} \right\}, \quad (6)$$

Here A^\dagger and A_S^\dagger are stable approximations of pseudo-inverses, for example, the filtered-backprojection (FBP) for X-ray CT imaging. In practice, we can always precompute $A^\dagger y$, and also predefine a set of N sketching operators S_1, S_2, \dots, S_N . In each of the training iterations of SGD or Adam, we randomly sample a S_i where $i \in [1, N]$ and compute an efficient approximate gradient. For structured inverse problems such as X-ray CT, we can observe significant computational acceleration via this form of sketching.

Although we mainly focus on sketching the vanilla form of EI regularization here, it is worth noting that the same idea can be easily extended to enhanced versions of EI with slight modifications, for example, the

Algorithm 1 Sketched Equivariant Imaging for Test-Time Network-Adaptation

- 1: **Inputs:** Observation y ; EI regularization parameter λ , number of iterations J ; network input z (default choice $z = A^\dagger y$)
 - 2: **Initialize:** Neural network \mathcal{F}_θ ;
 - 3: **For** $j = 1, \dots, J$ **do**:
 - 4: Obtain randomly sketched operators A_S, A_S^\dagger , sample $g \sim G$;
 - 5: Compute $x_1 = \mathcal{F}_\theta(z)$;
 - 6: Compute $x_2 = T_g(x_1)$;
 - 7: Compute $x_3 = \mathcal{F}_\theta(A_S^\dagger(A_S x_2))$;
 - 8: Update θ via progressively minimizing the loss $\mathcal{L} = \mathbb{E}_{g \sim G, S} \{ \|y_S - A_S x_1\|_2^2 + \lambda \|x_2 - x_3\|_2^2 \}$ using a gradient-based optimizer (such as Adam) in each iteration;
 - 9: **End For**
 - 10: $x^* = \mathcal{F}_{\theta^*}(z)$
-

robust EI regularizer (REI) proposed by (Chen et al., 2022) with simulated noise term ε introduced in every iteration to our regularizer $\mathbb{E}_{g \sim G, S, \varepsilon} \|T_g \mathcal{F}_\theta(A^\dagger y) - \mathcal{F}_\theta(A_S^\dagger(A_S T_g \mathcal{F}_\theta(A^\dagger y) + \varepsilon))\|_2^2$ according to the noise distribution.

We believe that the Sketched-EI regularization we proposed here is mostly valuable in test-time training for network-adaptation comparing to standard EI, since in such scenarios the practitioners particularly desire computational efficiency. Such test-time adaptation is vital in medical imaging as it mitigates distribution-shift and also boost the reconstruction performance. We present this EI-based test-time adaptation framework in Algorithm 1.

2.2 Parameter-Efficient Network Adaptation (NA) via Optimizing Only the Batch-Norms

The EI and Sketched-EI can both be applied to perform network adaptation (NA) at test time. Instead of training from scratch, we can initialize EI and Sketched EI directly with the pre-trained network. Network adaptation is a very important auxiliary post-processing technique for imaging inverse problems, as the reconstruction networks may often be applied to new problems which are out of their training distributions.

Since the network is pre-trained under the NA setting, there is hope that we can adjust a few crucial parameters/layers. Inspired by the works of Frankle et al. (2021); Mueller et al. (2024), we found an efficient approach for NA via only optimizing the BatchNorm (BN) layers for both EI and Sketched EI. The BN layers typically takes the form of:

$$N_{\theta_1, \theta_2}(v) = \frac{\theta_1(v - \mu)}{\sigma} + \theta_2 \quad (7)$$

where (θ_1, θ_2) are trainable parameters, where the statistics parameters (μ, σ) are automatically computed on the fly while training. For the U-Net architecture we are using for EI and Sketched EI in the experiments, there are 22 BN layers. As a result of applying BN-only optimization on EI and Sketched EI for network adaptation tasks, we derive and name our new approaches BN-NA-EI and Sketched BN-NA-EI, which are remarkably efficient for network adaptation tasks. The details can be found in Algorithm 2.

2.3 Extending Sketched EI with Coil Sketching for Computationally Efficient MRI

Taking into account the distinct properties of multi-coil MRI data (refer to Section 3.1 for details), we present a special sketched EI tailored for multi-coil data, utilizing coil sketching. We summarize the forward model

Algorithm 2 BatchNorm-only Sketched Equivariant Imaging for Efficient Network-Adaptation

- 1: **Inputs:** Observation y ; Equivariant strength parameter λ , number of iterations J ; network input z (default choice $z = A^\dagger y$) and a pretrained neural network \mathcal{F}_θ^* ;
 - 2: **For** $j = 1, \dots, J$ **do**:
 - 3: Obtain randomly sketched operators A_S, A_S^\dagger , sample $g \sim G$;
 - 4: Keep θ unchanged while only optimize the BatchNorm layers' parameters θ^{BN} ;
 - 5: Compute $x_1 = \mathcal{F}_{\theta^{\text{BN}}}(z)$;
 - 6: Compute $x_2 = T_g(x_1)$;
 - 7: Compute $x_3 = \mathcal{F}_{\theta^{\text{BN}}}(A_S^\dagger(A_S x_2))$;
 - 8: Update θ^{BN} via progressively minimizing the loss $\mathcal{L} = \mathbb{E}_{g \sim G, S} \{ \|y_S - A_S x_1\|_2^2 + \lambda \|x_2 - x_3\|_2^2 \}$ using a gradient-based optimizer (such as Adam) in each iteration;
 - 9: **End For**
 - 10: $x^* = \mathcal{F}_{\theta^*}(z)$
-

of MRI reconstruction as a linear model:

$$\mathbf{k} = \mathbf{M} \circ \mathbf{F}(\mathbf{C}\mathbf{x}),$$

where $\mathbf{k} \in \mathbb{C}^{CN}$ is a stack version of $\{\mathbf{k}_i \in \mathbb{C}^N\}_{i=1}^C$ as defined in Eq. (10), $\mathbf{x} \in \mathbb{C}^D$ is raw image. The matrices \mathbf{F} and \mathbf{C} are defined as follows:

$$\mathbf{C} = \begin{bmatrix} \text{diag}(C_1) \\ \vdots \\ \text{diag}(C_C) \end{bmatrix},$$

$$\mathbf{F} = \mathbf{I}_C \otimes \tilde{\mathbf{F}},$$

where \otimes is the Kronecker product, $\mathbf{C} \in \mathbb{C}^{CD \times D}$ represents the point-wise multiplication by the C -channel sensitivity maps. $\mathbf{F} \in \mathbb{C}^{CN \times CD}$ is a block diagonal matrix with C blocks $\{\tilde{\mathbf{F}} \in \mathbb{C}^{N \times D}\}$ that represents the Fourier transform. In addition, $\mathbf{I}_C \in \mathbb{R}^{C \times C}$ is the identity matrix. We will use the notation \mathbf{I}_a , where $a \in \mathbf{R}$, to refer to the identity matrix $a \times a$.

2.3.1 CLASSICAL SKETCHING

The classical sketching uses a randomly generated matrix $\mathbf{S} \in \mathbb{R}^{\hat{C}D \times CD}$ ($\hat{C} < C$), then the sketched forward model can be summarized as

$$\mathbf{k}^s = \mathbf{M}_s \circ \mathbf{F}_s(\mathbf{S}\mathbf{C}\mathbf{x})$$

where \mathbf{S} is block binary matrix with components \mathbf{S}_{ij} defined as

$$\mathbf{S}_{ij} = \begin{cases} \mathbf{1}, \\ \mathbf{0}, \end{cases}$$

where $\mathbf{0}, \mathbf{1} \in \mathbb{R}^{D \times D}$ are all-zero and all-one matrices. Figure 1 illustrates the concept of classical sketching.

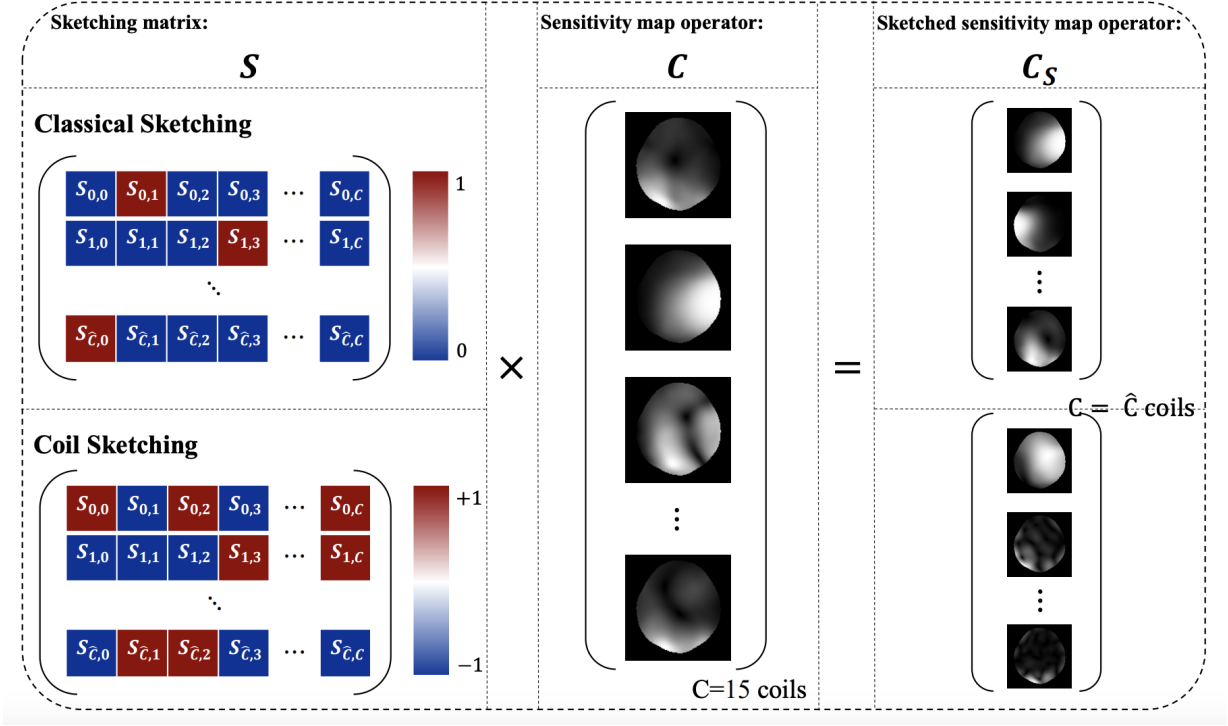


Figure 1: Structured sketching matrix of [Oscanoa et al. \(2024\)](#). The classical sketching matrix consists of a group binary mask, with each element being an all-ones matrix or an all-zeros matrix. Each row features exactly an all-ones matrix, and the remaining elements are all-zeros matrices. The coil sketching matrix, in contrast, comprises two blocks: one block is a group identity matrix (not shown in the figure), and the other block follows a group Rademacher distribution with probability $p = 0.5$ as showed in the figure

2.3.2 COIL SKETCHING

Inspired by the research findings of [Oscanoa et al. \(2024\)](#), this study considers integrating their proposed coil sketching algorithm with the Equivariant Imaging framework to develop a more efficient sketching solution for multi-coil MRI. Initially, the original multi-coil k -space data \mathbf{k} undergoes coil compression ([Buehrer et al., 2007](#)), with PCA (Principal Component Analysis) being the predominant approach ([Zhang et al., 2013](#); [Huang et al., 2008](#)) for compressing the resulting C -channel data:

$$\mathbf{k} = [\mathbf{k}_1, \mathbf{k}_2, \dots, \mathbf{k}_C],$$

where $\mathbf{k}_i = (k_i^1, k_i^2, \dots, k_i^n)^\top$, for each \mathbf{k}_i , subtracting its means, that is

$$\bar{\mathbf{k}}_i = \mathbf{k}_i - \frac{\sum_{j=1}^n k_i^j}{n}.$$

Then the covariance matrix V between the random variable components $\bar{\mathbf{k}}_i$ and $\bar{\mathbf{k}}_j$ can be accessed by

$$v_{ij} = \text{cov}(\bar{\mathbf{k}}_i, \bar{\mathbf{k}}_j) = \frac{\text{conj}(\bar{\mathbf{k}}_i^\top) \bar{\mathbf{k}}_j}{n-1},$$

where $\text{conj}(\cdot)$ means conjugate operation. Subsequently, the eigenvectors and eigenvalues of V are obtained, and Q is defined as a matrix where the eigenvectors of V form the columns. For coil compression, the largest L eigenvectors are utilized to construct a new matrix Q_L , which serves as the compression matrix to reduce the C vectors to the L vectors ($L \leq C$). Finally, coil compression is applied to the original k -space data as follows:

$$(\tilde{\mathbf{k}}_1, \tilde{\mathbf{k}}_2, \dots, \tilde{\mathbf{k}}_L) = (\mathbf{k}_1, \mathbf{k}_2, \dots, \mathbf{k}_C) \cdot Q_L.$$

Research on coil compression has indicated that many low-energy virtual coils can be omitted with minimal impact on image quality (Buehrer et al., 2007; Zhang et al., 2013; Huang et al., 2008). Hence, the coil sketching algorithm proposes that a sketching matrix specifically designed to minimize information loss in high-energy virtual coils, while targeting low-energy coil data, would yield a superior approximation compared to a design that reduces information indiscriminately across all virtual coils. In addition, the corresponding coil sensitivity maps are estimated using the widely used method ESPIRiT (Uecker et al., 2014).

We define $R \in \mathbb{R}$ as the number of high-energy virtual coils and $S \in \mathbb{R}$ as the number of sketched low-energy coils incorporated in the sketched coil sensitivity map operator $\mathbf{C}_S = \tilde{\mathbf{S}}\mathbf{C}$. The sketching matrix $\tilde{\mathbf{S}} \in \mathbb{R}^{\hat{C}D \times CD}$ satisfies $\hat{C} \leq L \leq C$, and it follows that $\hat{C} = R + S$. Now, $\tilde{\mathbf{S}}$ has the following form:

$$\tilde{\mathbf{S}} = \begin{bmatrix} \mathbf{I}_R & \mathbf{0} \\ \mathbf{0} & \tilde{\mathbf{S}}_S \end{bmatrix},$$

where $\tilde{\mathbf{S}}_S \in \mathbb{R}^{S \times (C-R)}$ is a random matrix with i.i.d. entries, and $\mathbf{0}$ are zero matrices. Specifically, for the probability density function for the random entries of $\tilde{\mathbf{S}}_S$, we consider Rademacher distribution ($\{+1, -1\}$ entries with equal probability $p = 0.5$) as suggested in Oscanoa et al. (2024). The detailed algorithm can be found in Algorithm 3 and Figure 1.

2.4 Theoretical Analysis

For a proof-of-concept, we provide following bound for the proposed sketching scheme, demonstrating that our sketched EI regularizer is an effective approximation of the original EI.

Theorem 1 (Approximation bound for Sketched EI regularization) *Suppose the network \mathcal{F}_θ is L -Lipschitz, while $\|v\|_2 \leq r$, we have:*

$$\|v - \mathcal{F}_\theta(A^\dagger Av)\|_2 - Lr\delta \leq \|v - \mathcal{F}_\theta(A_S^\dagger A_S v)\|_2 \leq \|v - \mathcal{F}_\theta(A^\dagger Av)\|_2 + Lr\delta \quad (8)$$

almost surely, where δ is a constant only depending on the sketch size m and the choice of sketching operator, and we denote here $v := T_g \mathcal{F}_\theta(A^\dagger y)$.

We provide the proof of this theorem in the Appendix. The L -Lipschitz continuity assumption of the form:

$$\|\mathcal{F}_\theta(p) - \mathcal{F}_\theta(q)\|_2 \leq L\|p - q\|_2, \quad \forall p, q \in \mathcal{X} \quad (9)$$

on the reconstruction network \mathcal{F}_θ is standard for the theoretical analysis of deep networks in imaging inverse problems. For example, in the convergence analysis of plug-and-play algorithms (Ryu et al., 2019; Tan et al., 2024) and diffusion-based MCMC (Cai et al., 2024), such types of assumptions have been used in pre-trained denoisers or generative image priors based on deep networks for convergence proofs. The above theorem provides an upper bound and a lower bound that sandwich the sketched EI regularization with the original EI regularization, with a deviation δ that scales approximately as $O(1/\sqrt{m})$.

Algorithm 3 Sketched-EI for Multi-coil MRI with Coil sketching

- 1: **Inputs:** k -space measurements $\mathbf{k} = [\mathbf{k}_1, \dots, \mathbf{k}_C]$; EI regularization parameter λ ;
 - 2: **Initialize:** Set parameters L, \hat{C}, R and S , neural network \mathcal{F}_θ ;
 - 3: **for** $i = 1, \dots, C$ **do**
 - 4: $\bar{\mathbf{k}}_i = \mathbf{k}_i - \frac{\sum_{i=j}^n k_i^j}{n}$
 - 5: **end for**
 - 6: Compute covariance matrix V between $\bar{\mathbf{k}}_i$ and $\bar{\mathbf{k}}_j$;
 - 7: Define Q_L as the biggest L eigenvectors of V ;
 - 8: Compute $\hat{\mathbf{k}}_L = \mathbf{k} \cdot Q_L = [\tilde{\mathbf{k}}_1, \dots, \tilde{\mathbf{k}}_L]$;
 - 9: Estimate the corresponding sensitivity maps \mathbf{C}_L of the compressed k -space data $\hat{\mathbf{k}}_L$ with ESPIRiT;
 - 10: Form sketched sensitivity maps with \hat{C} coils: $\mathbf{C}_S = \hat{\mathbf{S}} \cdot \mathbf{C}_L$.
 - 11: Obtain sketched forward Fourier operator and inverse Fourier operator: $A_S = M_s \circ F_s \mathbf{C}_S$, $A_S^\dagger = (M_s \circ F_s)^{-1}$, $y_S = \hat{\mathbf{k}}_L$, by default: $z = A^\dagger y$;
 - 12: **For** $j = 1, \dots, J$ **do**:
 - 13: Sample $g \sim G$
 - 14: Compute $x_1 = \mathcal{F}_\theta(z)$;
 - 15: Compute $x_2 = T_g(x_1)$;
 - 16: Compute $x_3 = \mathcal{F}_\theta(A_S^\dagger(A_S x_2))$;
 - 17: Update θ via progressively minimizing the loss $\mathcal{L} = \mathbb{E}_{g \sim G} \{\|y_S - A_S x_1\|_2^2 + \lambda \|x_2 - x_3\|_2^2\}$ using a gradient-based optimizer (such as Adam) in each iteration;
 - 18: **End For**
-

In the appendix, we demonstrate that the theoretical approximation accuracy can be significantly improved for approximately low-rank measurement operators, which have fast decaying spectrum. This observation is consistent with the findings of Tang et al. (2020) on suitable imaging applications of stochastic optimization. In the work of Tang et al. (2020), it has been demonstrated both theoretically and numerically that stochastic gradient methods can only be effective for those inverse problems for which the measurement operator A has a fast decaying spectrum (approximately low-rank) structure. For example, X-ray CT, multicoil MRI, and PET are all very good applications of stochastic gradient methods with minibatch sampling, while they all have fast decaying spectrum. Our theory here suggests that we should expect similar behavior for our Sketched EI regularization.

This theoretical result, although preliminary and motivational, justifies that the proposed sketching scheme provides a good approximation for the original EI regularizer statistically and admits a nice mathematical interpretation.

3. Numerical Experiments

In this section, we show numerically the performance of the proposed method for the sparse-view CT image reconstruction and multi-coil MRI reconstruction problems.

3.1 Setup and Implementation

Sparse-view CT imaging We evaluate the proposed method on the *sparse-view CT image reconstruction* task, wherein the forward operator $A \in \mathbb{R}^{m \times n}$ ($m < n$) is underdetermined and has a non-trivial nullspace

\mathcal{N}_A . In particular, the imaging physics of X-ray computed tomography (CT) is modeled by the discrete `radon` transform, with A defined accordingly; 100 scans (angles) are uniformly subsampled to produce the sparse-view sinograms (observations) denoted as y . The filter back projection (FBP) function (i.e., `iradon`) is employed to compute a stable approximation of A^\dagger . The aim of this task is to recover a ground truth image x^* from a single observation y . To this end, we integrate the rotational invariance inherent in CT images into a deep image prior framework, where \mathcal{G} represents the group of rotations spanning from 1 to 360 degrees (with $|\mathcal{G}| = 360$). A single sample from the CT100 dataset (Clark et al., 2013) is resized to 512×512 pixels, and the `radon` function is subsequently applied to generate the corresponding 100-scan sinogram.

Accelerated Multi-coil MRI imaging MRI produces images of biological tissues by sampling the Fourier transform (k -space) of the image \mathbf{x} , where the k -space samples refer to frequency-domain measurements and k is the spatial wave number. The forward operator is $A := M \circ \mathcal{F}$ where \mathcal{F} is the 2D Fourier transform and M is a binary mask operator for accelerating, whose values correspond to the measured frequencies. In the multi-coil MRI literature, the k -space samples measured by each coil are modulated by their sensitivity map to the MR signal arising from different regions. In particular, the k -space sample measured by the i -th coil is

$$\mathbf{k}_i = M \circ \mathcal{F}(C_i \mathbf{x}), \quad i = 1, 2, \dots, N, \quad (10)$$

where C_i is a complex-valued diagonal matrix encoding the position dependent sensitivity map of the i -th coil and N is the number of coils. The pseudo-inverse $A^\dagger = \mathcal{F}^{-1} \circ M$ is the masked inverse Fourier transform. In this task, we exploit the invariance of MRI images in rotation and use rotations of integer degree ($|\mathcal{G}| = 360$). The single multi-coil MRI data were obtained from NYU fastMRI Initiative (Zbontar et al., 2018) with originally 15 coils, and resize it to 320×320 pixels. We trained in the measurement of 15 coils at $4\times$ acceleration. We use complex-valued data treating the real and imaginary parts of the images as separate channels. For the purpose of visualization, we display only the magnitude image.

Throughout both experiments, we used a U-Net (Ronneberger et al., 2015) to build \mathcal{F}_θ as suggested in Chen et al. (2021). We compare our method (Sketched EI) with two different learning strategies: the unsupervised deep image prior approach with the loss function (3); unsupervised deep image prior term with the equivariance regularized term (EI-DIP) as shown in (4). For a fair comparison with the sketched EI, we use the residual U-Net architecture for all counterpart learning methods to ensure that all methods have the same inductive bias from the neural network architecture.

We demonstrate that the sketched operation is straightforward and can be easily extended to existing deep models without modifying the architectures. All of our experiments were performed with a NVIDIA RTX 4060ti GPU, alongside with `DeepInv` toolbox¹. All the compared methods are implemented in PyTorch and optimized by Adam (Kingma and Ba, 2015), for which we set the learning rate to 5×10^{-4} . We train all comparing methods over 5,000 iterations for CT and 10,000 iterations for MRI.

3.2 Numerical Results

We conduct comparative numerical studies of our proposed sketched EI-DIP method against traditional methods such as DIP, as well as the deep image prior with state-of-the-art equivariant regularizer (Chen et al., 2021), EI-DIP. To ensure a fair comparison, all parameters involved in the deep image prior and the EI method are either manually tuned to optimality or automatically selected as described in the references.

1. <https://deepinv.github.io/deepinv/>

We present our results with detailed descriptions in the following figures and tables which demonstrate the effectiveness of our sketched EI scheme.

3.2.1 SPARSE-VIEW CT

We first evaluate the performance of Sketched EI using a single sample from the resized *sparse-view CT 100* dataset, and then further compare this method to DIP and EI. For the EI-DIP method, we use the architecture suggested in [Chen et al. \(2021\)](#) to achieve the best performance, and we build the DIP using the same residual U-Net used in EI. For the sketched EI, we choose the subsampling sketch as our S , which splits the measurement operator into N minibatches, $A_{S_1}, A_{S_2}, \dots, A_{S_N}$ from interleaved angles. In each iteration, we randomly select one of the minibatch and perform the update. We test on the choices $N = 2, 5, 10, 20$ respectively here. As shown in [Figure 2](#), the baseline DIP frameworks deliver only modest reconstruction fidelity in our study, while the introduction of the EI regularizer improves reconstruction precision. In particular, the sketch-guided EI model with $N = 10$ achieves the highest reconstruction quality of all the evaluated methods. In order to further study the impacts of the sketching operation, we performed ablation experiments with four different sketch sizes as reported in [Figure 3](#) and [Figure 4\(a\)](#). We can observe that the results for Sketched EI are slightly better than full EI, for the number of minibatch splits chosen to be either 2, 5, 10 or 20 (corresponds to 50%, 20%, 10% and 5% of origin, respectively), and reaches the best at splits 10. The result would deteriorate if we choose to sketch over aggressively (20 splits in this setting), indicating a phase transition.

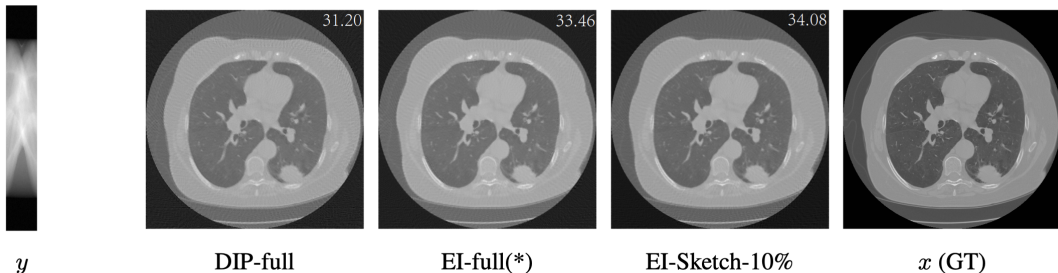


Figure 2: CT Images (with corresponding PSNR) reconstructed by DIP, EI-DIP and our Sketched EI-DIP. DIP-full and EI-DIP-full use 100 CT scans, while EI-DIP-Sketch-10% means only 10% of 100 CT scans used per iteration. (*) denotes the baseline.

[Figure 4\(b\)](#) illustrates that all methods achieve a significant decrease in mean square error (MSE) within the first 2,000 seconds of training. The Sketched EI surpasses the vanilla EI (EI-DIP-full) in convergence rate, achieving a faster decline in MSE. Furthermore, among the sketched schemes employing minibatch splits of 2, 5, 10, and 20, the split-10 scheme demonstrates the most pronounced and rapid convergence.

We further investigate the application of Sketched EI method to network adaptation ([Zhang and Gao, 2024](#)) (also known as test time training) task, which involves adjusting a pre-trained model to accommodate variations in new data or tasks. Specifically, we applied the model pre-trained ² using the first 90 samples of *CT 100* dataset to reconstruct an unseen CT image (index 95 sample in *CT 100* dataset) using only noisy measurement with a known Gaussian noise level of 0.1, with the experimental results presented in top row of [Figure 5](#). The visualized results of the network adaptation experiments demonstrate that the sketched EI method achieves comparable reconstruction performance compared to the standard EI method

2. <https://drive.google.com/drive/folders/1Io0quD-RvoVNkCmE36aQYpouuEAEp5pF>

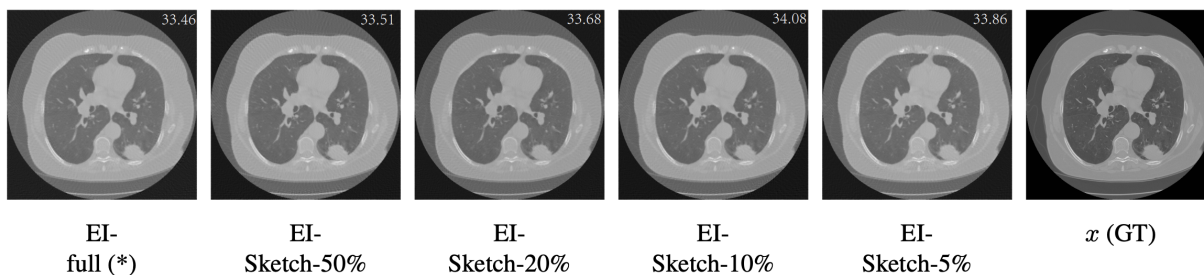
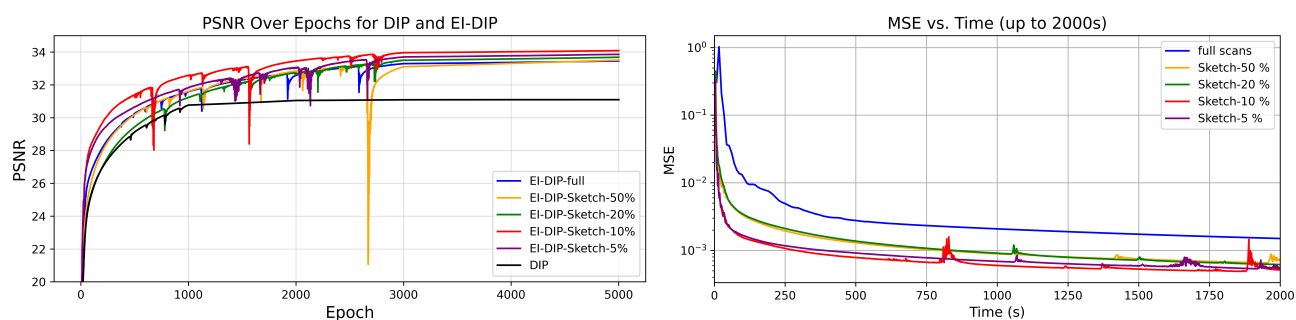


Figure 3: CT Images (with corresponding PSNR) reconstructed by Sketched EI, with different sketch sizes. EI-DIP-full uses 100 CT scans, while 50%, 20%, 10% and 5% means only 50%, 20%, 10% and 5% of 100 CT scans used per iteration. (*) denotes the baseline.



(a): Reconstruction accuracy curves for all the compared schemes

(b): MSE variation with time up to 2000 seconds of the proposed EI-DIP with different sketched size

Figure 4: PSNR and MSE comparisons of the proposed Sketched EI-DIP and DIP methods. EI-DIP-full uses 100 CT scans, while 50%, 20%, 10% and 5% means only 50%, 20%, 10% and 5% of 100 CT scans used per iteration

without sketching, while reaching superior reconstructions compared to their counterparts without network adaptation.

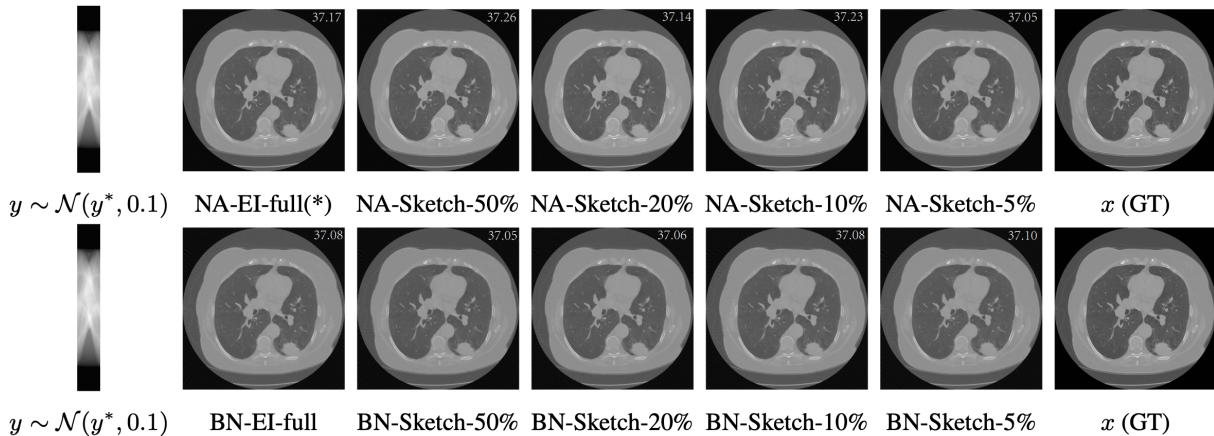
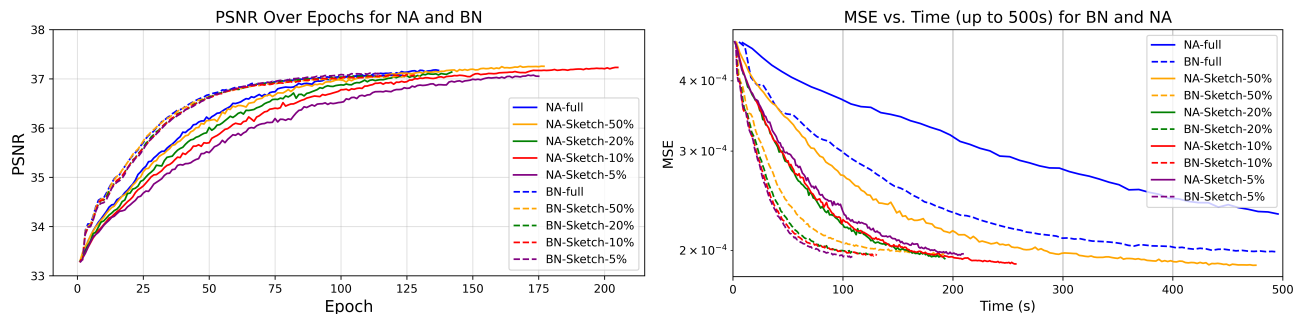


Figure 5: CT image reconstructions by Sketched EI-DIP in Network Adaptation task with a single noisy measurement. Top row shows reconstructions of fine-tuning entire network (NA) while bottom row fine-tuning only the BatchNorm (BN) layers, both with various sketch size. NA(BN)-full uses 100 CT scans, while 50%, 20%, 10% and 5% means only 50%, 20%, 10% and 5% of 100 CT scans used per iteration. (*) denotes the baseline.



(a): Trend of PSNR with epoch in Network Adaptation and BatchNorm only schemes

(b): Trend of MSE with time (up to 500 seconds) in Network Adaptation and BatchNorm only schemes

Figure 6: Curves of PSNR and MSE of Network Adaptation and BatchNorm only schemes in CT reconstruction by Sketched EI-DIP. NA(BN)-full uses 100 CT scans, while 50%, 20%, 10% and 5% means only 50%, 20%, 10% and 5% of 100 CT scans used per iteration

Inspired by Frankle et al. (2021), we fixed all other model parameters during the network adaptation process, fine-tuning only the BatchNorm layer parameters. The results, as shown in Figure 5, indicate that fine-tuning the entire model outperforms fine-tuning only the BatchNorm layers for the network adaptation task, while both fine-tuning schemes achieve superior performance than their counterparts by direct training. We continue by providing some insights of both two fine-tuning methods by comparing their convergence speeds. Figure 6(a) shows that BatchNorm only scheme converges faster than fine-tuning the entire layers, while both methods required significantly less computation time to achieve superior performance compared

to the directly trained counterparts. Moreover, the sketch operation further speeds up the convergence in both methods, as illustrated in Figure 6(b).

	PSNR	Time (s) / Epoch	Trainable Param ($\times 10^7$)	Training Epochs
Full-parameter NA				
	(noise level 0.1)			
EI-full (*)	37.17	9.56	3.45	137
EI-Sketch-50%	37.26	2.66	3.45	177
EI-Sketch-20%	37.14	1.34	3.45	142
EI-Sketch-10%	37.23	1.25	3.45	205
EI-Sketch-5%	37.05	1.18	3.45	175
BatchNorm-Only NA				
	(noise level 0.1)			
BN-EI-full	37.08	5.45	0.0014	125
BN-EI-Sketch-50%	37.05	1.46	0.0014	130
BN-EI-Sketch-20%	37.06	1.09	0.0014	114
BN-EI-Sketch-10%	37.08	1.00	0.0014	128
BN-EI-Sketch-5%	37.10	0.95	0.0014	115

Table 1: Further comparisons between Network Adaptation and BatchNorm only schemes in CT reconstruction, from the prospective of efficiency. EI-DIP-full uses 100 CT scans, while 50%, 20%, 10% and 5% means only 50%, 20%, 10% and 5% of 100 CT scans used per iteration. (*) denotes the baseline.

To better understand the benefits of the Network Adaptation and BatchNorm Only fine-tuning schemes, Table 1 summarizes the results of these two competing schemes in noisy measurement with noise level of $\sigma = 0.1$. As we can see from Table 1, the time consumption per iteration was massively decreased with the sketch operation, while with increasing sketch size, the time consumption did not decrease significantly anymore. In addition, the memory cost was roughly half the way down with the increasing sketch size. The training parameters used in the BatchNorm only scheme were significantly reduced, as can be anticipated.

PSNR \ Scheme	NA-EI					BN-EI				
	*full (100)	50%	20%	10%	5%	full (100)	50%	20%	10%	5%
noise level										
Sketch-size										
0.05	37.48	37.46	37.30	37.23	37.05	37.18	37.17	37.08	37.15	37.11
0.2	36.81	36.51	36.70	36.19	36.52	36.52	36.72	36.54	36.76	36.73
0.5	35.34	35.25	34.89	34.45	34.71	35.59	35.48	35.59	35.52	35.51

Table 2: PSNR of CT reconstructions by Sketched EI in Network Adaptation and BatchNorm only schemes with increasing noise level from $\sigma = 0.05$ to 0.5. 'full' means using 100 CT scans, while 50%, 20%, 10% and 5% means only 50%, 20%, 10% and 5% of 100 CT scans used per iteration. * denotes the baseline.

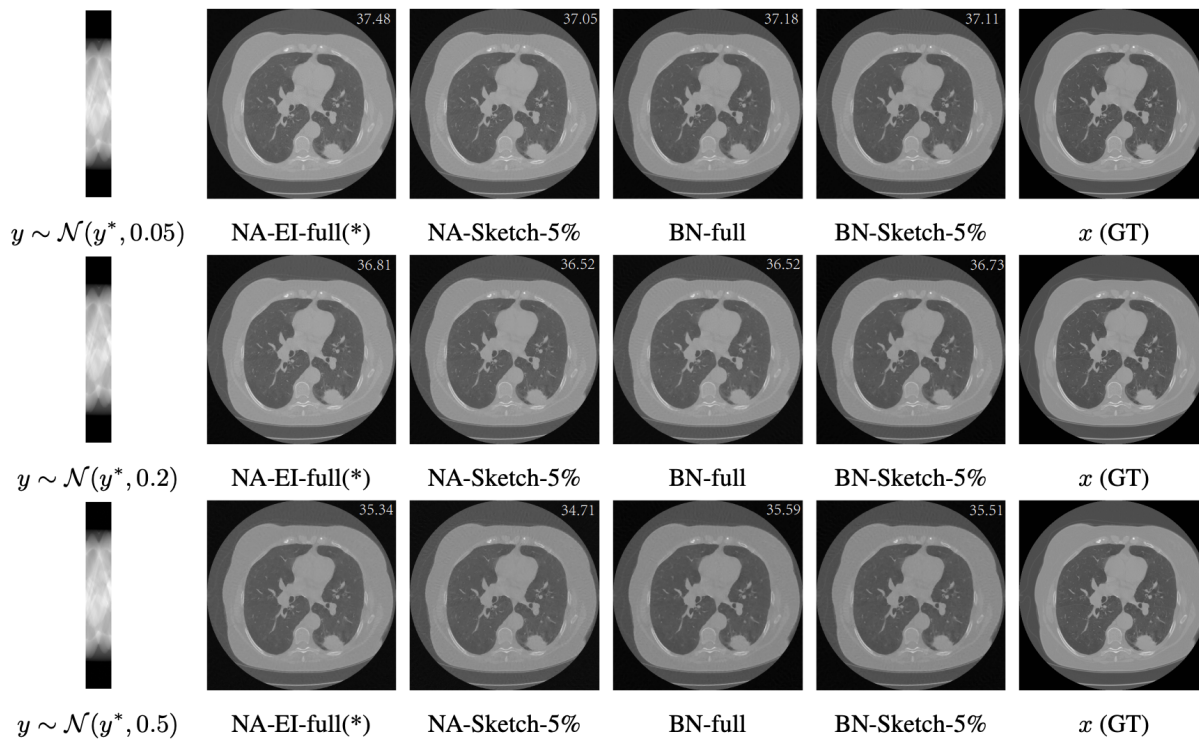


Figure 7: CT image reconstructions by Sketched EI-DIP of Network Adaptation (NA) and BatchNorm only (BN) schemes with different noise level and different sketch size. NA(BN)-full uses 100 CT scans, while Sketch-5% means only 5% of 100 CT scans used per iteration. (*) denotes the baseline.

As the noise level increases, both fine-tuning schemes exhibit performance degradation to varying extents (Table 2, Figure 7). The Network Adaptation scheme demonstrates markedly higher sensitivity to noise than the BatchNorm-only scheme. Moreover, larger sketch sizes exacerbate performance loss in the Network Adaptation scheme, whereas the BatchNorm-only scheme remains comparatively robust.

3.2.2 ACCELERATED MULTI-COIL MRI

Another experiment provides an initial demonstration of equivariant imaging for multi-coil MRI reconstruction problem. We evaluated the performance of two distinct sketched EI-DIP methods proposed in this study for multicoil MRI, using a knee MRI image with 15 coils from Zbontar et al. (2018). Subsequently, we perform a comparative analysis of the reconstruction results under two distinct sketch schemes and varying sketch sizes. Consistent with Section 3.2.1, we begin by comparing our proposed methods with the vanilla DIP method, considering the same DIP network architectures as outlined in Section 3.2.1.

For Coil-Sketch and Classical-Sketch methods, S is defined as the sketch operation that samples $N \leq 15$ coils from original 15 coils, then forms a minibatch named A_{S_N} . However, these two sketch schemes differ in their minibatch partition strategies. Specifically, as described in Algorithm 3, Coil-Sketch compresses the initial 15 coils and then selects the first L compressed virtual coils as the new multi-coils. Subsequently, the first R higher-energy virtual coils are retained, while the last S lower-energy virtual coils undergo sketch operation. In contrast, Classical-Sketch directly acts on the original 15 coils, randomly sampling N coils into a minibatch. During each iteration, the minibatch is randomly chosen from the 15 coils for updates. For this study, we experiment with $N = 10, 5$, and 2, respectively.

The visualized comparisons are shown in Figure 8, as can be seen, the performance of the DIP methods is still suboptimal, consistent with findings from the sparse-view CT experiments. In comparison, the EI-DIP method achieves remarkable improvements in reconstruction quality due to the EI regularizer. Furthermore, the reconstruction results produced by these two proposed sketch methods exhibit almost no loss in performance and even surpass the vanilla EI-DIP method. Furthermore, as presented in Figure 10 (b), the time cost per iteration of the sketched EI-DIP decreased compared to the vanilla EI-DIP method. Specifically, Coil-Sketch-2 decreased 19% per iteration compared to vanilla EI-DIP, while the Classical-Sketch-2 decreased 17%.

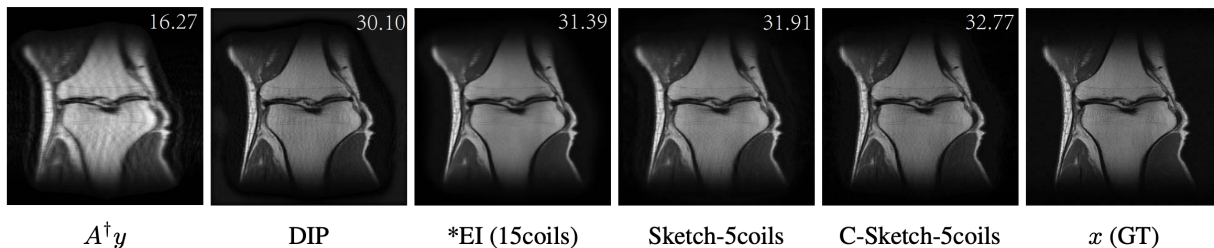


Figure 8: Multi-coil MRI Images (with corresponding PSNR) reconstructed by DIP, EI-DIP and our two Sketched EI-DIP methods, where ‘Sketch’ shorts for classical-sketch and ‘C-Sketch’ for coil-sketch. ‘*’ denotes the baseline.

To further explore our schemes, we performed ablation studies with three different sketch sizes in two different sketch methods, as visualized in Figure 9 and Figure 10(a). The results show that for coil-sketch, performance improves markedly when the sketch size increases to 5 but decreases slightly when the size reaches 2. Nevertheless, all three sketch sizes outperform vanilla EI-DIP, attributed to the sketch algorithm optimized for multi-coil MRI. In contrast, for classical-sketch, performance initially increases with smaller

sketch sizes but significantly deteriorates once the size reaches 2, performing much worse than vanilla EI-DIP. Besides, as presented in Figure 10(a), compared to the vanilla EI-DIP method, both sketch methods converge faster in first 300 seconds of training. In particular, the coil-sketch method converges even more dramatically than classical-sketch while maintaining performance levels far exceeding vanilla EI-DIP. Both schemes reach their own fastest convergence when the sketch size is 10.

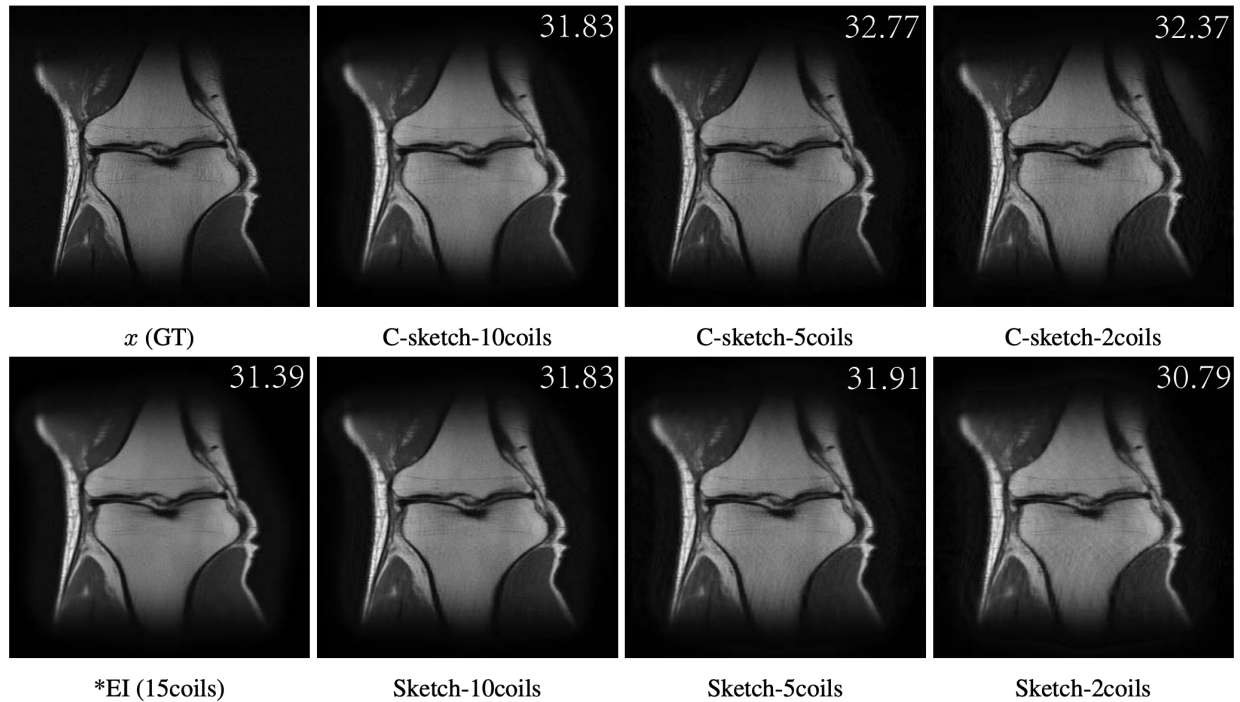


Figure 9: Multi-coil MRI Images (with corresponding PSNR) reconstructed by Sketched EI-DIP, with different sketch sizes, and ‘Sketch’ shorts for classical-sketch, ‘C-sketch’ stands for coil-sketch. ‘*’ denotes the baseline.

Next, we investigate the performance of our proposed Coil-Sketched EI in Network Adaptation task. Specifically, we fine-tune the model trained³ on the fastMRI knee dataset in Darestani et al. (2022), with the experimental results illustrated in Figure 11. As we can see, the single measurement was disrupted by Gaussian noise with noise level $\sigma = 0.005$, and the visualized images indicate that, in both the full-parameter Network Adaptation (NA) and BatchNorm-only (BN) NA scenarios, our proposed method yields reconstruction results that remain comparable to those obtained under noiseless conditions (as illustrated by comparing Figure 9 with Figure 11), even in the presence of noise. Additionally, the coil sketching operation appears to have minimal influence on reconstruction quality when noisy measurements are used, regardless of the fine-tuning strategy employed.

To gain deeper understanding, we proceed by comparing convergence speeds and efficiency of these two fine-tuning strategies. As shown in Figure 12, under the early stopping strategy, the BatchNorm-only (BN) scheme converges more rapidly than the Network Adaptation (NA) scheme, although NA ultimately

3. <https://drive.usercontent.google.com/download?id=1Hmm5QvnMD41QlSMx7OMZTbQ4-1g9Tvw3&export=download&authuser=0>

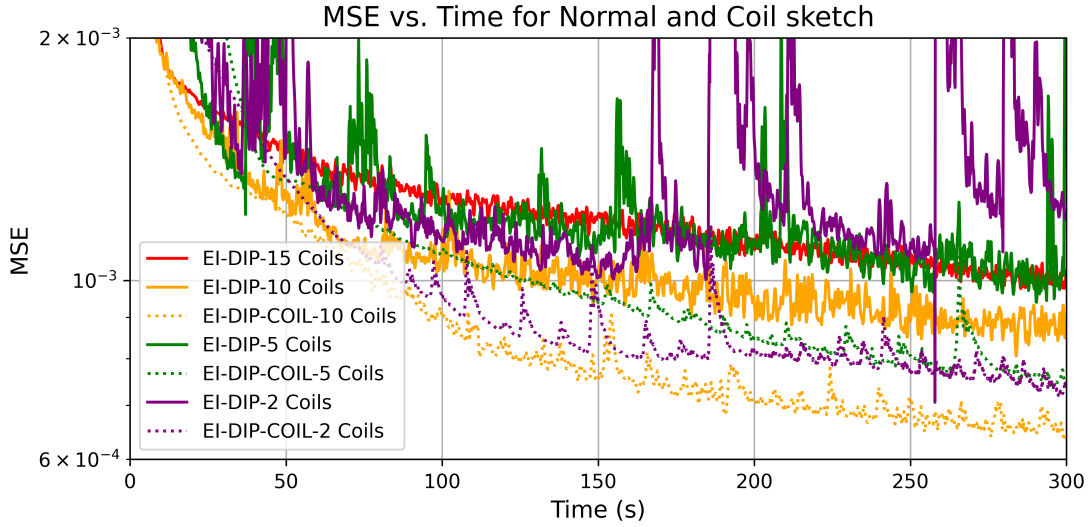


Figure 10: MSE variation with time up to 300 seconds of the proposed EI-DIP with different sketched size for both classical sketch and coil sketch schemes. The red-curve (EI-DIP-15 coils) denotes the baseline.

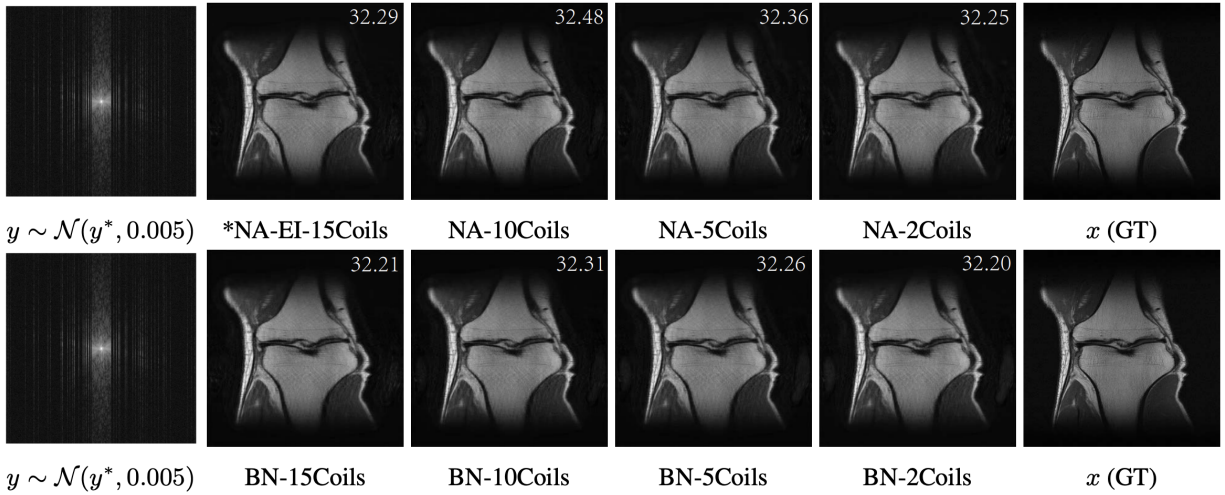
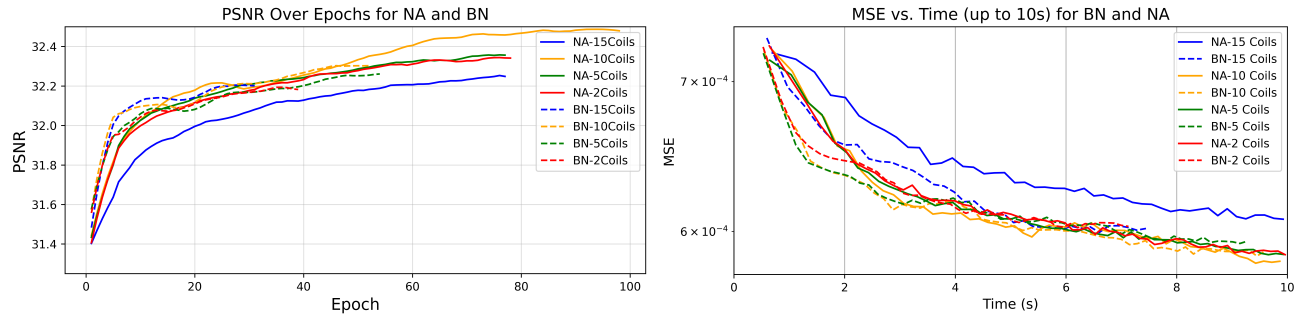


Figure 11: Multi-coil MRI image reconstructions in Network Adaptation task with a single noisy measurement (noise level $\sigma = 0.005$). Top row shows reconstructions of fine-tuning entire network (NA) while bottom row fine-tuning only the BatchNorm (BN) layers, both with various sketch size. ‘*’ denotes the baseline.

yields superior reconstruction results. Additionally, both NA and BN schemes demonstrate robustness to the sketching operation, as evidenced in Figure 12.



(a): Trend of PSNR with epoch in NA and BN schemes

(b): Trend of MSE with time (up to 10 seconds) in Network Adaptation and BatchNorm only schemes

Figure 12: Curves of PSNR and MSE of Network Adaptation (NA) and BatchNorm only (BN) schemes in multi-coil MRI reconstruction. The solid blue curve (NA-15Coils) denotes the baseline.

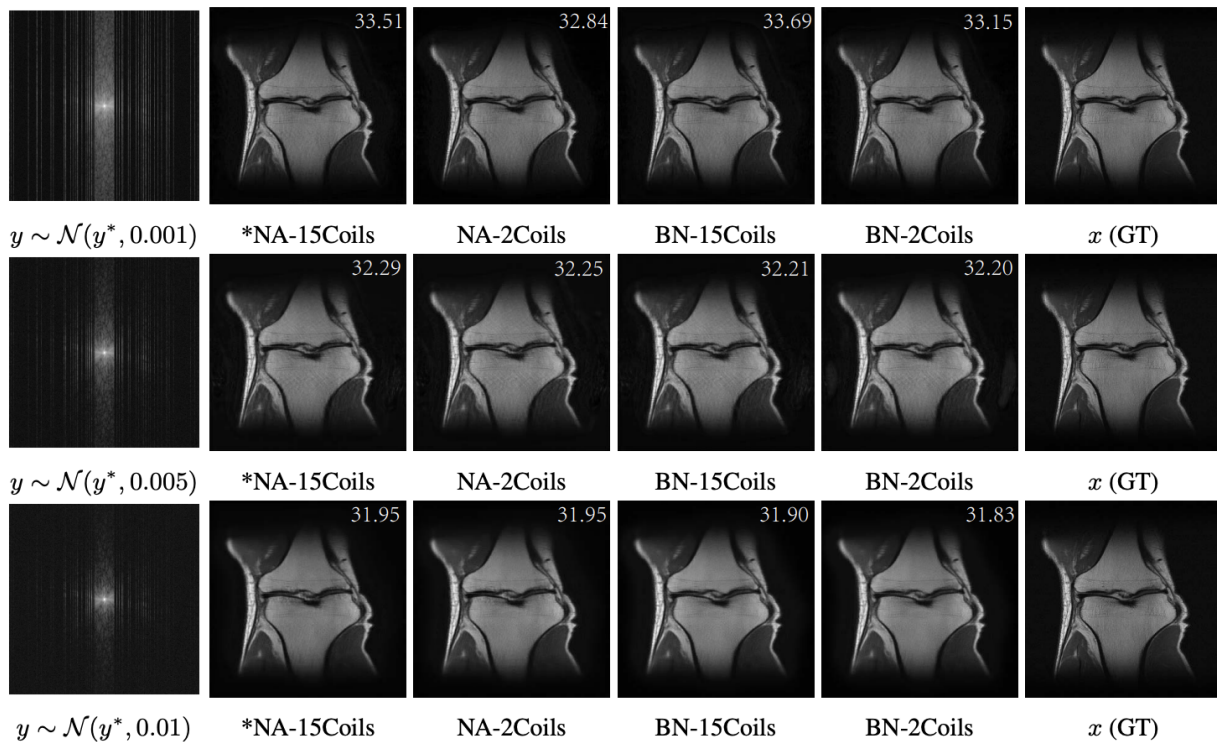


Figure 13: Multi-coil MRI image reconstructions of Network Adaptation (NA) and BatchNorm only (BN) schemes with different noise level and different sketch size. '*' denotes the baseline.

We further evaluated the performance of the two fine-tuning schemes, Network Adaptation (NA) and BatchNorm-only (BN), across varying noise levels, as shown in Figure 13 and Table 3. The results indi-

PSNR \ Scheme	NA-EI				BN-NA-EI				
	noise level	15(*)	10	5	2	15	10	5	2
Coil numbers		15(*)	10	5	2	15	10	5	2
0.001		33.51	33.02	32.95	32.84	33.69	33.08	33.10	33.15
0.01		31.95	31.70	31.69	31.95	31.90	31.82	31.86	31.83

Table 3: PSNR of multi-coil MRI reconstructions in Network Adaptation and BatchNorm only schemes with increasing noise level from $\sigma = 0.001$ to 0.01. (*) denotes the baseline.

cate that the performance of both methods gradually declines as the noise level increases. Notably, both approaches present robustness to the sketching operation at different noise levels.

4. Conclusion

In this work, we propose a sketched EI regularizer which can be efficiently applied for unsupervised training of deep imaging networks, especially in the real-time test-time training / network-adaptation setting. We provide a motivational theoretical analysis of the proposed sketching scheme demonstrating that it is an effective approximation of the original EI regularization proposed by [Chen et al. \(2021\)](#). In test-time training setting, we compare our Sketched EI approach with standard EI for sparse-view X-ray CT imaging tasks, and observe a substantial acceleration. Moreover, for network adaptation of pre-trained models, we discovered a powerful acceleration scheme which optimizes only on the normalization layers for both EI and Sketched EI. Finally, we propose an extension of our schemes using coil-sketching tailored for multi-coil MRI and observe significantly improved reconstruction speed and performance compared to standard approaches.

5. Appendix

In this appendix we provide the proof for the motivational bound presented in Theorem 1 for the approximation of EI regularizer. We start by proving the upper bound:

$$\begin{aligned}
\|v - \mathcal{F}_\theta(A_S^\dagger A_S v)\|_2 &= \|v - \mathcal{F}_\theta(A_S^\dagger A_S v) + \mathcal{F}_\theta(A^\dagger A v) - \mathcal{F}_\theta(A^\dagger A v)\|_2 \\
&\leq \|v - \mathcal{F}_\theta(A^\dagger A v)\|_2 + \|\mathcal{F}_\theta(A_S^\dagger A_S v) - \mathcal{F}_\theta(A^\dagger A v)\|_2.
\end{aligned}
\tag{11}$$

Due to the assumption on the L -Lipschitz continuity of the network, we have

$$\begin{aligned}
&\|\mathcal{F}_\theta(A_S^\dagger A_S v) - \mathcal{F}_\theta(A^\dagger A v)\|_2 \\
&\leq L \|A_S^\dagger A_S v - A^\dagger A v\|_2 \\
&\leq L \|A^\dagger S^\dagger S A - A^\dagger A\|_2 \|v\|_2 \\
&\leq L \|A^\dagger (S^T S - I) A\|_2 \|v\|_2 \\
&\leq L r \|A^T (S^T S - I) A\|_2
\end{aligned}
\tag{12}$$

The remaining challenge is to bound the term $\|A^T(S^T S - I)A\|_2 \leq \delta$ almost surely, which actual value is dependent on the choice of sketching operator M . Here we illustrate with the choice of sub-Gaussian sketches, while subsampling and randomized orthogonal sketches also satisfy the bound with different values of δ and probability. According to (Pilanci and Wainwright, 2015, Proposition 1), if M is a σ -sub-Gaussian sketch with sketch size m , we have:

$$Lr\|A^T(S^T S - I)A\|_2 \leq Lr\delta, \quad (13)$$

with:

$$\delta = c_0\sqrt{\frac{d}{m}} + \delta_0 \quad (14)$$

with probability at least $1 - \exp(-c_1\frac{m\delta_0^2}{\sigma^4})$ where c_0, c_1 are universal constants. We hence finish the proof of the upper bound. For the lower bound, we use the same reasoning:

$$\begin{aligned} \|v - \mathcal{F}_\theta(A^\dagger Av)\|_2 &= \|v - \mathcal{F}_\theta(A_S^\dagger A_S v) + \mathcal{F}_\theta(A_S^\dagger A_S v) - \mathcal{F}_\theta(A^\dagger Av)\|_2 \\ &\leq \|v - \mathcal{F}_\theta(A_S^\dagger A_S v)\|_2 + \|\mathcal{F}_\theta(A_S^\dagger A_S v) - \mathcal{F}_\theta(A^\dagger Av)\|_2 \\ &\leq \|v - \mathcal{F}_\theta(A_S^\dagger A_S v)\|_2 + Lr\delta \end{aligned} \quad (15)$$

Then immediately we have $\|v - \mathcal{F}_\theta(A_S^\dagger A_S v)\|_2 \geq \|v - \mathcal{F}_\theta(A^\dagger Av)\|_2 - Lr\delta$. Thus finishes the proof.

Special case of low-rank operators. We can have tighter bounds if the measurement operator A has additional structures. For instance, if A has rank $k \ll d$, let's write the SVD as $A = U\Sigma V^T$ with semi-unitary matrices $U \in \mathbb{R}^{n \times k}$, $V^T \in \mathbb{R}^{k \times d}$ such that $U^T U = V^T V = I$, and diagonal matrix $\Sigma \in \mathbb{R}^{k \times k}$ whose diagonal contains the non-zero singular values $\Sigma = \text{diag}[\sigma_1, \dots, \sigma_k]$, we have:

$$\begin{aligned} &\|\mathcal{F}_\theta(A_S^\dagger A_S v) - \mathcal{F}_\theta(A^\dagger Av)\|_2 \\ &\leq L\|A^\dagger(S^T S - I)A\|_2\|v\|_2 \\ &\leq Lr\|A^T(AA^T)^{-1}(S^T S - I)A\|_2 \\ &= Lr\|V\Sigma U^T U\Sigma^{-2}(S^T S - I)U\Sigma V^T\|_2 \\ &= Lr\|V\Sigma^{-1}(S^T S - I)U\Sigma V^T\|_2 \\ &\leq \frac{Lr\sigma_1}{\sigma_k}\|U^T(S^T S - I)U\|_2 \end{aligned} \quad (16)$$

Then we only need $\delta = c_0\sqrt{\frac{k}{m}} + \delta_0$ for Theorem 1 to hold.

Regarding approximately low-rank operators. In real-world applications, such as tomographic imaging (CT/MRI/PET), the measurement operator are approximately low-rank. For instance, the spectrum of k -approximate low-rank operator being $\Sigma = \text{diag}[\sigma_1, \dots, \sigma_k, \dots, \sigma_{\min}]$, where $\sigma_1 = O(1)$, $\sigma_k = O(1)$, $\sigma_{k-1} = o(1)$, $\sigma_{\min} = o(1)$, then the above bound would be:

$$\|\mathcal{F}_\theta(A_S^\dagger A_S v) - \mathcal{F}_\theta(A^\dagger Av)\|_2 \leq O(1)\|U^T(S^T S - I)U\|_2 + o(1). \quad (17)$$

Considering the results for low-rank and approximate low-rank cases, we can observe that as long as the measurement operator A has fast decaying spectrum, where $k \ll d$, then the approximation of the sketched EI regularizer can be accurate.

References

- Shady Abu-Hussein, Tom Tirer, Se Young Chun, Yonina C Eldar, and Raja Giryes. Image restoration by deep projected gsure. In *Proceedings of the IEEE/CVF Winter Conference on Applications of Computer Vision*, pages 3602–3611, 2022.
- Riccardo Barbano, Johannes Leuschner, Maximilian Schmidt, Alexander Denker, Andreas Hauptmann, Peter Maass, and Bangti Jin. An educated warm start for deep image prior-based micro ct reconstruction. *IEEE Transactions on Computational Imaging*, 8:1210–1222, 2022.
- Joshua Batson and Loic Royer. Noise2self: Blind denoising by self-supervision. In *International Conference on Machine Learning*, pages 524–533, 2019.
- A. Beck and M. Teboulle. Fast gradient-based algorithms for constrained total variation image denoising and deblurring problems. *IEEE Transactions on Image Processing*, 18(11):2419–2434, 2009.
- Martin Buehrer, Klaas P. Pruessmann, Peter Boesiger, and Sebastian Kozerke. Array compression for mri with large coil arrays. *Magnetic Resonance in Medicine*, 57(6):1131–1139, 2007. doi: <https://doi.org/10.1002/mrm.21237>. URL <https://onlinelibrary.wiley.com/doi/abs/10.1002/mrm.21237>.
- Ziruo Cai, Junqi Tang, Subhadip Mukherjee, Jinglai Li, Carola-Bibiane Schönlieb, and Xiaoqun Zhang. Nf-ula: Normalizing flow-based unadjusted langevin algorithm for imaging inverse problems. *SIAM Journal on Imaging Sciences*, 17(2):820–860, 2024.
- Marcello Carioni, Subhadip Mukherjee, Hong Ye Tan, and Junqi Tang. Unsupervised approaches based on optimal transport and convex analysis for inverse problems in imaging. *Radon Series on Computational and Applied Mathematics*, 2024.
- Dongdong Chen, Julián Tachella, and Mike E Davies. Equivariant imaging: Learning beyond the range space. In *Proceedings of the IEEE/CVF International Conference on Computer Vision*, pages 4379–4388, 2021.
- Dongdong Chen, Julián Tachella, and Mike E Davies. Robust equivariant imaging: a fully unsupervised framework for learning to image from noisy and partial measurements. In *Proceedings of the IEEE/CVF Conference on Computer Vision and Pattern Recognition*, pages 5647–5656, 2022.
- Kenneth Clark, Bruce Vendt, Kirk Smith, John Freymann, Justin Kirby, Paul Koppel, Stephen Moore, Stanley Phillips, David Maffitt, Michael Pringle, et al. The cancer imaging archive (tcia): maintaining and operating a public information repository. *Journal of digital imaging*, 26:1045–1057, 2013.
- Mohammad Zalbagi Darestani, Jiayu Liu, and Reinhard Heckel. Test-time training can close the natural distribution shift performance gap in deep learning based compressed sensing. In *International conference on machine learning*, pages 4754–4776. PMLR, 2022.
- Matthias J Ehrhardt, Zeljko Kereta, Jingwei Liang, and Junqi Tang. A guide to stochastic optimisation for large-scale inverse problems. *arXiv preprint arXiv:2406.06342*, 2024.
- Jonathan Frankle, David J. Schwab, and Ari S. Morcos. Training batchnorm and only batchnorm: On the expressive power of random features in {cnn}s. In *International Conference on Learning Representations*, 2021. URL <https://openreview.net/forum?id=vYeQQ29TbvX>.

- Feng Huang, Sathya Vijayakumar, Yu Li, Sarah Hertel, and George R. Duensing. A software channel compression technique for faster reconstruction with many channels. *Magnetic Resonance Imaging*, 26(1):133–141, 2008. ISSN 0730-725X. doi: <https://doi.org/10.1016/j.mri.2007.04.010>. URL <https://www.sciencedirect.com/science/article/pii/S0730725X07002731>.
- Rie Johnson and Tong Zhang. Accelerating stochastic gradient descent using predictive variance reduction. In *Advances in neural information processing systems*, pages 315–323, 2013.
- Diederik P Kingma and Jimmy Ba. Adam: A method for stochastic optimization. *Proceedings of 3rd International Conference on Learning Representations*, 2015.
- Jaakko Lehtinen, Jacob Munkberg, Jon Hasselgren, Samuli Laine, Tero Karras, Miika Aittala, and Timo Aila. Noise2noise: Learning image restoration without clean data. *arXiv preprint arXiv:1803.04189*, 2018.
- Jiaming Liu, Yu Sun, Xiaojian Xu, and Ulugbek S Kamilov. Image restoration using total variation regularized deep image prior. In *ICASSP 2019-2019 IEEE International Conference on Acoustics, Speech and Signal Processing (ICASSP)*, pages 7715–7719. Ieee, 2019.
- Jiaming Liu, Yu Sun, Cihat Eldeniz, Weijie Gan, Hongyu An, and Ulugbek S Kamilov. Rare: Image reconstruction using deep priors learned without groundtruth. *IEEE Journal of Selected Topics in Signal Processing*, 14(6):1088–1099, 2020.
- Gary Mataev, Peyman Milanfar, and Michael Elad. Deepred: Deep image prior powered by red. In *Proceedings of the IEEE/CVF International Conference on Computer Vision Workshops*, pages 0–0, 2019.
- Perla Mayo, Matteo Cencini, Carolin M Pirkl, Marion I Menzel, Michela Tosetti, Bjoern H Menze, and Mohammad Golbabaee. Stodip: Efficient 3d mrf image reconstruction with deep image priors and stochastic iterations. In *International Workshop on Machine Learning in Medical Imaging*, pages 128–137. Springer, 2024.
- Maximilian Mueller, Tiffany Vlaar, David Rolnick, and Matthias Hein. Normalization layers are all that sharpness-aware minimization needs. *Advances in Neural Information Processing Systems*, 36, 2024.
- Julio A. Oscanoa, Frank Ong, Siddharth S. Iyer, Zhitao Li, Christopher M. Sandino, Batu Ozturkler, Daniel B. Ennis, Mert Pilanci, and Shreyas S. Vasanawala. Coil sketching for computationally efficient mr iterative reconstruction. *Magnetic Resonance in Medicine*, 91(2):784–802, 2024. doi: <https://doi.org/10.1002/mrm.29883>. URL <https://onlinelibrary.wiley.com/doi/abs/10.1002/mrm.29883>.
- M. Pilanci and M. J. Wainwright. Randomized sketches of convex programs with sharp guarantees. *Information Theory, IEEE Transactions on*, 61(9):5096–5115, 2015.
- Mert Pilanci and Martin J Wainwright. Newton sketch: A near linear-time optimization algorithm with linear-quadratic convergence. *SIAM Journal on Optimization*, 27(1):205–245, 2017.
- Olaf Ronneberger, Philipp Fischer, and Thomas Brox. U-net: Convolutional networks for biomedical image segmentation. In Nassir Navab, Joachim Hornegger, William M. Wells, and Alejandro F. Frangi, editors, *Medical Image Computing and Computer-Assisted Intervention – MICCAI 2015*, pages 234–241, Cham, 2015. Springer International Publishing. ISBN 978-3-319-24574-4.

- Alessandro Rudi, Raffaello Camoriano, and Lorenzo Rosasco. Less is more: Nyström computational regularization. *Advances in neural information processing systems*, 28, 2015.
- Ernest Ryu, Jialin Liu, Sicheng Wang, Xiaohan Chen, Zhangyang Wang, and Wotao Yin. Plug-and-play methods provably converge with properly trained denoisers. In *International Conference on Machine Learning*, pages 5546–5557, 2019.
- Jérémy Scanvic, Mike Davies, Patrice Abry, and Julián Tachella. Self-supervised learning for image super-resolution and deblurring. *arXiv preprint arXiv:2312.11232*, 2023.
- Imraj Singh, Riccardo Barbano, Zeljko Kereta, Bangti Jin, Kris Thielemans, and Simon Arridge. 3d pet-dip reconstruction with relative difference prior using a sirf-based objective. Fully3D, 2023.
- Yu Sun, Brendt Wohlberg, and Ulugbek S Kamilov. An online plug-and-play algorithm for regularized image reconstruction. *IEEE Transactions on Computational Imaging*, 2019.
- Julián Tachella, Junqi Tang, and Mike Davies. The neural tangent link between cnn denoisers and non-local filters. *IEEE/CVF Conference on Computer Vision and Pattern Recognition*, 2021.
- Julián Tachella, Dongdong Chen, and Mike Davies. Sensing theorems for unsupervised learning in linear inverse problems. *Journal of Machine Learning Research*, 24(39):1–45, 2023.
- Julián Tachella, Mike Davies, and Laurent Jacques. Unsure: Unknown noise level stein’s unbiased risk estimator. *arXiv preprint arXiv:2409.01985*, 2024.
- Hong Ye Tan, Subhadip Mukherjee, Junqi Tang, and Carola-Bibiane Schönlieb. Provably convergent plug-and-play quasi-newton methods. *SIAM Journal on Imaging Sciences*, 17(2):785–819, 2024.
- Junqi Tang, Mohammad Golbabaee, and Mike E Davies. Gradient projection iterative sketch for large-scale constrained least-squares. In *International Conference on Machine Learning*, pages 3377–3386. PMLR, 2017.
- Junqi Tang, Karen Egiazarian, Mohammad Golbabaee, and Mike Davies. The practicality of stochastic optimization in imaging inverse problems. *IEEE Transactions on Computational Imaging*, 6:1471–1485, 2020.
- Tom Tirer, Raja Giryes, Se Young Chun, and Yonina C Eldar. Deep internal learning: Deep learning from a single input. *IEEE Signal Processing Magazine*, 41(4):40–57, 2024.
- Martin Uecker, Peng Lai, Mark J. Murphy, Patrick Virtue, Michael Elad, John M. Pauly, Shreyas S. Vasanawala, and Michael Lustig. Espirit—an eigenvalue approach to autocalibrating parallel mri: Where sense meets grappa. *Magnetic Resonance in Medicine*, 71(3):990–1001, 2014. doi: <https://doi.org/10.1002/mrm.24751>. URL <https://onlinelibrary.wiley.com/doi/abs/10.1002/mrm.24751>.
- Dmitry Ulyanov, Andrea Vedaldi, and Victor Lempitsky. Deep image prior. In *Proceedings of the IEEE Conference on Computer Vision and Pattern Recognition*, pages 9446–9454, 2018.
- Andrew Wang and Mike Davies. Fully unsupervised dynamic mri reconstruction via diffeo-temporal equivariance. *arXiv preprint arXiv:2410.08646*, 2024a.

- Andrew Wang and Mike Davies. Perspective-equivariant imaging: an unsupervised framework for multi-spectral pansharpening. *arXiv preprint arXiv:2403.09327*, 2024b.
- Jure Zbontar, Florian Knoll, Anuroop Sriram, Tullie Murrell, Zhengnan Huang, Matthew J Muckley, Aaron Defazio, Ruben Stern, Patricia Johnson, Mary Bruno, et al. fastmri: An open dataset and benchmarks for accelerated mri. *arXiv preprint arXiv:1811.08839*, 2018.
- Lei Zhang and Xinbo Gao. Transfer adaptation learning: A decade survey. *IEEE Transactions on Neural Networks and Learning Systems*, 35(1):23–44, 2024. doi: 10.1109/TNNLS.2022.3183326.
- Tao Zhang, John M. Pauly, Shreyas S. Vasanawala, and Michael Lustig. Coil compression for accelerated imaging with cartesian sampling. *Magnetic Resonance in Medicine*, 69(2):571–582, 2013. doi: <https://doi.org/10.1002/mrm.24267>. URL <https://onlinelibrary.wiley.com/doi/abs/10.1002/mrm.24267>.